Journal of ELECTRONIC MATERIALS, Vol. 38, No. 8, 2009
DOI: 10.1007/s11664-009-0793-4
© 2009 TMS
Special Issue Paper

Flexibility of *p–n* Junction Formation from SWIR to LWIR Using MBE-Grown $Hg_{(1-x)}Cd_xTe$ on Si Substrates

M.F. VILELA,[1,2] S.F. HARRIS,[1] R.E. KVAAS,[1] A.A. BUELL,[1] M.D. NEWTON,[1] K.R. OLSSON,[1] D.D. LOFGREEN,[1] and S.M. JOHNSON[1]

1.—Raytheon Vision System (RVS), 75 Coromar Drive, Goleta, CA 93117, USA. 2.—e-mail: mauro_f_vilela@raytheon.com

In this paper, we show the versatility of using molecular-beam epitaxy (MBE) for the growth of the mercury cadmium telluride (HgCdTe) system. Abrupt composition profiles, changes in doping levels or switching doping types are easily performed. It is shown that high-quality material is achieved with $Hg_{(1-x)}Cd_xTe$ grown by MBE from a cadmium mole fraction of $x = 0.15$ to $x = 0.72$. Doping elements incorporation as low as 10^{15} cm^{-3} for both *n*-type and *p*-type material as well as high incorporation levels $>10^{18}$ cm^{-3} for both carrier types were achieved. X-ray curves, secondary-ion mass spectrometry (SIMS) data, Hall data, the influence of doping incorporation with cadmium content and growth rate, etch pit density (EPD), composition uniformity determined from Fourier-transform infrared (FTIR) transmission spectroscopy, and surface defect maps from low to high x values are presented to illustrate the versatility and quality of HgCdTe material grown by MBE. All data presented in this work are from layers grown on silicon (112) substrate.

Key words: HgCdTe, HgCdTe/Si, molecular-beam epitaxy (MBE), *n*-type, *p*-type, doping, Hall, SIMS, EPD

INTRODUCTION

$Hg_{(1-x)}Cd_xTe$, mercury cadmium telluride (HgCdTe), is the ideal choice for multicolor infrared focal-plane arrays (FPAs), large-format FPAs, avalanche photodiodes (APD) arrays, and for many applications that require devices with a response from short-wavelength infrared (SWIR) through very long-wavelength infrared (VLWIR). The band gap of this semiconductor material can be easily modified from near 0 eV to 1.6 eV by varying the Cd mole fraction of the $Hg_{(1-x)}Cd_xTe$ material being grown. The MBE growth technique appears to be an excellent match to this material family because it allows the fabrication of very complex devices and affords respectable latitude for designing the structures. MBE is a very powerful growth technique, and the ultrahigh-vacuum (UHV) environment enables the use of tools for growth control unmatched by any other growth technique. Residual gas analysis (RGA), reflection high-energy electron diffraction (RHEED), pyrometry, and spectroscopic ellipsometry (SE) are a few of the tools available for *in situ* monitoring which allow for real-time growth control. MBE also allows for the use of large-area substrates and/or multiple wafers for the growth. The traditional lattice-matched growth substrate, cadmium zinc telluride (CZT), is extremely expensive, has limited size (currently available up to 80 mm × 80 mm), and has a limited number of suppliers. Alternative substrates are explored to increase the growth area and lower the cost. Several alternative substrates have been studied as a replacement for CZT: silicon (Si), gallium arsenide (GaAs), sapphire, indium antimonide (InSb), and germanium (Ge). Si is the natural choice when taking into consideration pricing, available sizes, mature technology, and compatibility with readouts for infrared focal-plane array use. Raytheon has developed capability for both 100-mm and 150-mm Si substrates. The large lattice mismatch of silicon

(Received January 20, 2009; accepted March 30, 2009; published online April 21, 2009)

with HgCdTe (~19%) and the mismatch in thermal expansion coefficients (~2×) can cause HgCdTe epitaxial layers to relax by forming a network of misfit dislocations at the strained interface, giving typical EPD values in the mid to high 10^6 cm^{-2} range.

The main goal of this work is to demonstrate that the properties needed by most optoelectronic devices can be achieved when using HgCdTe-on-Si MBE technology. Early in the development process, we needed to verify that we are able to achieve required doping levels, both n-type and p-type, in a fashion that results in high growth yield. Large changes in concentration have to be easily achievable, from very low ($<10^{15}$ cm^{-3}) to very high concentrations ($>10^{18}$ cm^{-3}). They must also be abrupt and no cross-contamination should be observed. A low-background doping deposition system is also a must for high-performance devices. Crystal quality should be verified by narrow x-ray rocking curves, quantified by full-width at half-maximum (FWHM) values. In addition, a low threading dislocation density has to be assured in order to make possible devices whose operation is based on minority carrier transport, such as photovoltaic devices.

EXPERIMENT

All heteroepitaxial layers (ZnTe, CdTe, HgCdTe) were deposited in a 125-mm Riber Epineat MBE system using CdTe, ZnTe, and Te solid sources and a Raytheon-built liquid-Hg source which can be refilled without breaking the main vacuum chamber. Elemental indium for n-type and arsenic for p-type sources are used for doping materials. The 100-mm-diameter Si (112) substrates are prepared for growth using a hydrofluoric acid-based process. After the wet etch, wafers are loaded in a UHV introduction chamber prior to the growth. A ZnTe/CdTe buffer layer and HgCdTe device structures are then grown without wafer removal from the MBE system. All growth is performed in a rotating manipulator. Each growth begins with a buffer layer consisting of about 0.5 μm of ZnTe and 2 μm to 9 μm of CdTe. Early studies have demonstrated that the ZnTe initiation layer is important to preserve the substrate orientation, either (100)[1] or in the present case (112)B,[2] before the CdTe layer is grown. This serves to attenuate the propagating threading dislocation defects. A schematic of a single p–n HgCdTe structure is shown in Fig. 1 with some growth conditions displayed.

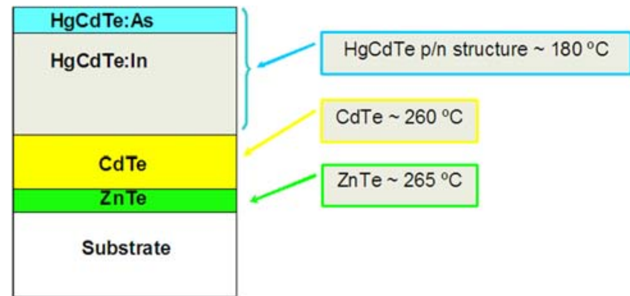

Fig. 1. Schematic of a single p–n HgCdTe structure grown on Si (112). Temperatures shown in this figure are approximate and measured by an optical pyrometer.

RESULTS AND DISCUSSION

A great deal of effort was spent to control key growth parameters in order to guarantee the uniformity, quality, and reproducibility of any layer grown. The two key parameters are growth temperature and source beam flux stability. These parameters are closely interrelated and were previously discussed for MWIR detectors[3]; now we will extend the discussions from SWIR to LWIR.

CONTROL OF COMPOSITION AND GROWTH RATE

Precise run-to-run control of composition as well as growth rate and doping requires good knowledge of each MBE source's material beam flux characteristics. In order to minimize any variation in flux due to cell aging, material displacement inside the source or source temperature oscillation, we measure fluxes for each cell at a fixed temperature prior to each growth using a nude ion gauge placed in front of the substrate manipulator. In addition, we use an *in situ* spectroscopic ellipsometer (SE), an M-2000 from J. A. Woollam Co., Inc. to control material composition in real time.[3] By using FTIR we have previously shown how powerful the MBE technique is by demonstrating in a larger production MBE system that very large-area devices can be routinely obtained with excellent lateral composition uniformity. For a full 150-mm Si wafer,[4] the uniformity is better than 1%. In this work, using a smaller Epineat MBE system, uniformity better than 5% from center to edge was consistently obtained. We also have utilized RHEED patterns to determine the optimal growth temperatures and fluxes.[3] A 15-kV STAIB electron gun was used that is protected with a gate valve to isolate it from the system when not in use. In addition, the electron gun is equipped with an extra flange allowing differential pumping, which minimizes effects of the high Hg pressure.

X-RAY ROCKING CURVES

The (422) FWHM x-ray rocking curve was used to monitor the crystal quality of our grown material. We use Cu K_α radiation from a Bede D1 system and a θ–2θ measurement. The FWHM of our HgCdTe on Si substrates is very consistent in the 80 arcsec to 100 arcsec range, independent of the x value (from $x = 0.16$ to 0.38), demonstrating the high structural quality of the material. We do not have any x-ray measurements for x values higher than 0.38, but EPD measurements for HgCdTe with x values varying from 0.15 to 0.72 all have similar values around 2.0×10^6 cm^{-2}, demonstrating equivalent

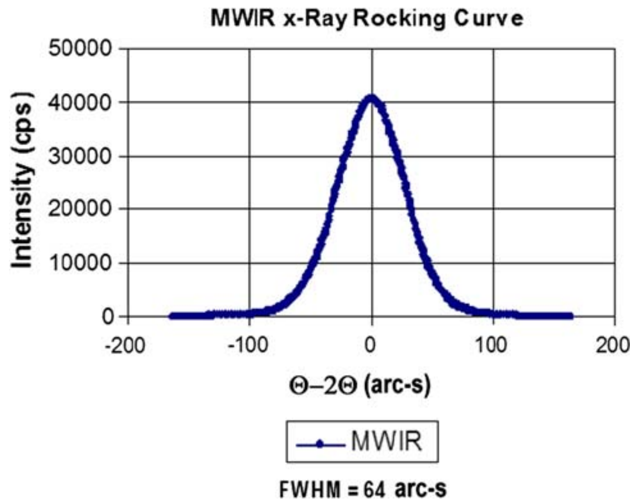

Fig. 2. X-ray rocking curve of a MWIR HgCdTe single layer grown on Si (112).

crystal quality, as discussed below. A MWIR HgCdTe/Si single layer with a FWHM of 64 arcsec is shown in Fig. 2 to demonstrate the high quality of our epitaxial material. A control wafer that had only the buffer layer grown on it (ZnTe + CdTe) had a FWHM of 80 arcsec.

HgCdTe/Si DEFECT DENSITY

Threading dislocation segments and macroscopic defects that are manifested as morphological defects on the surface of a HgCdTe film grown on a silicon substrate are the two most important classes of defects that affect the performance of IR detectors. Particulates, voids, and microvoids are easily detected by optical microscopy. Effects of these defects on device performance have already been reported.[5,6] The mechanism of formation and cause of defects are very complex and diverse. Different authors and groups agree that voids and microvoids are directly related to Hg fluxes and substrate growth temperature.[7–9] A thermodynamic approach for void and microvoid prevention can be found in Ref. 10. In order to assess the defect density in our wafers after growth, we use the August Technology NSX105 automated defect inspection system as described in Ref. 11, which gives full wafer mapping. Figure 3 shows an August defect map of a full two-color mid–long infrared detector structure. For properly adjusted growth conditions, we observe a defect density <100 cm^{-2} as shown in the August defect map displayed in Fig. 4 for a short-wave structure with a Cd mole fraction of $x = 0.72$.

The large lattice mismatch and differences in physical properties between Si and II–VI materials causes an increased threading dislocation density and can be readily measured by subjecting the film to a wet chemical etch that preferentially decorates threading segments intersecting the surface of the film through the formation of pits. We typically observe an EPD in the mid 10^6 cm^{-2} range for our structures from SWIR to LWIR HgCdTe/Si layers. Independent of the x value, the EPD decreases monotonically from high 10^7 cm^{-2} to low 10^6 cm^{-2} with increasing combined ZnTe/CdTe buffer layer thickness. This EPD value is still high when compared with EPD of similar structures grown on lattice-matched CZT substrates, which are in the low to mid 10^4 cm^{-2} range. However, this higher value of EPD on structures grown on Si substrates has not compromised the performance of detectors in the mid–long infrared spectrum.[3,12]

n- AND p-TYPE DOPING

One of the most important properties of a semiconductor material is the ability to incorporate both types of electrical carriers, n and p. Additionally, the ability to achieve an abrupt transition between the dopant species is important. The MBE technique and the HgCdTe system are a good match for

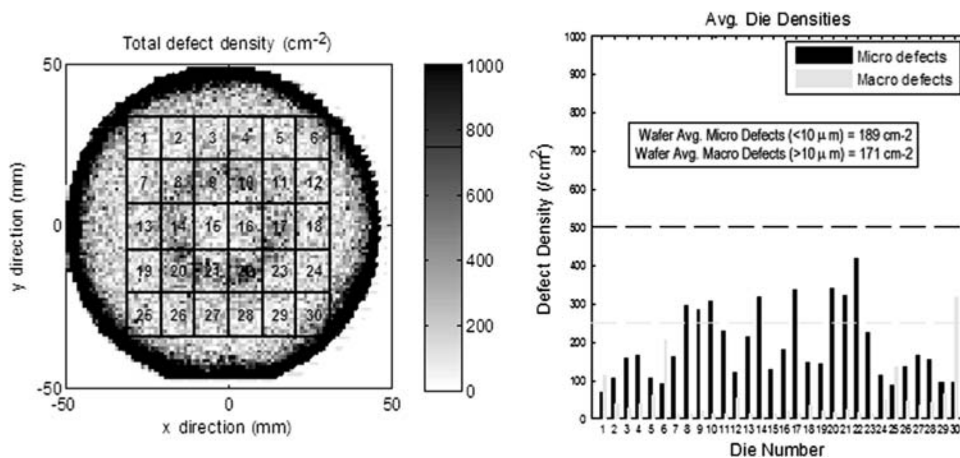

Fig. 3. August defect map of a full two-color mid-long infrared detector structure. (a) A 6 × 5 array is laid down on the surface and (b) total defect density of each individual bin from the array is shown: microdefects in black and macrodefects in light gray. Microdefects are those smaller than 10 μm in diameter and macrodefects are those larger than 10 μm in diameter.

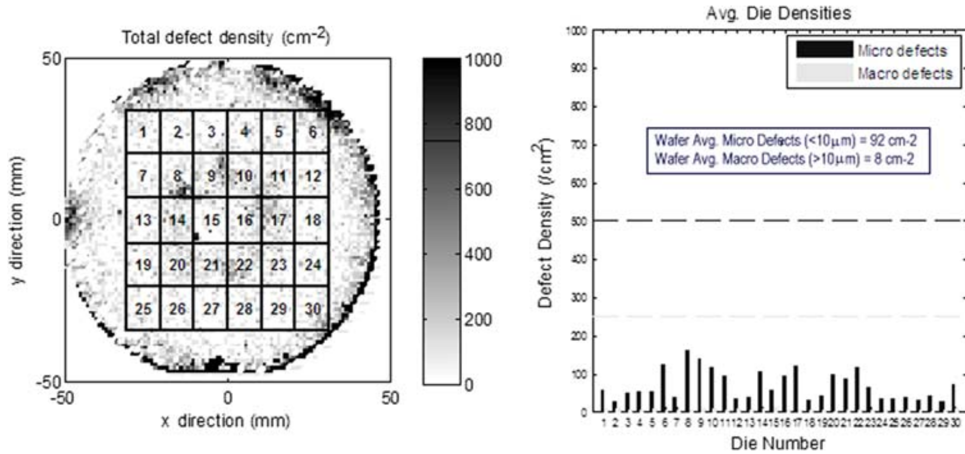

Fig. 4. August defect map of a short-wave infrared detector structure. (a) A 6 × 5 array is laid down on the surface and (b) total defect density of each individual bin from the array is shown: microdefects in black and macrodefects in light gray. Microdefects are those smaller than 10 μm in diameter and macrodefects are those bigger than 10 μm in diameter.

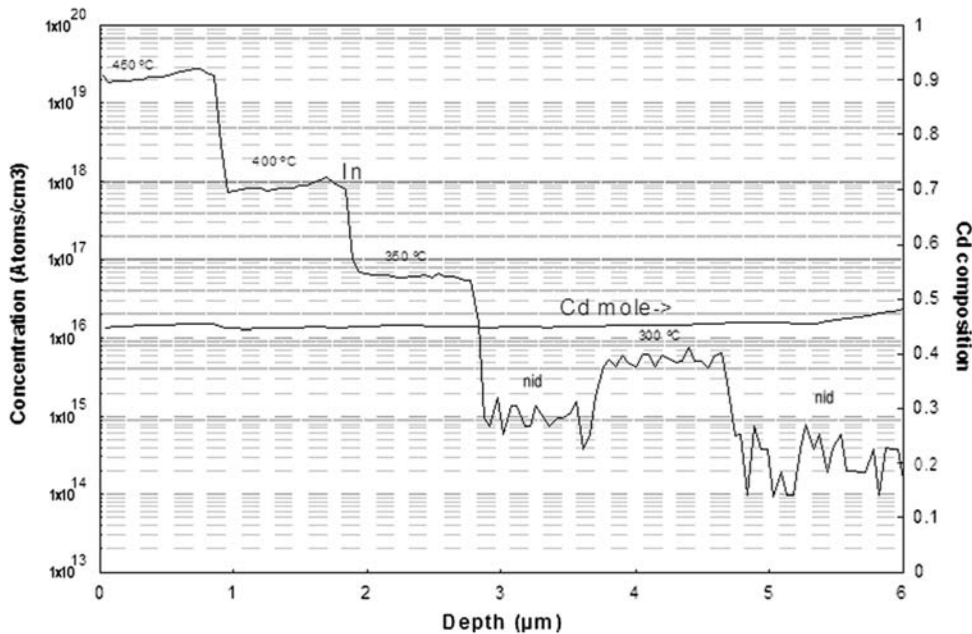

Fig. 5. SIMS scan from a calibration layer of indium doping for long-wave infrared material. *nid* = nonintentionally doped. The higher background level observed for a depth from 2.8 μm to 3.8 μm is due to the temperature increase in the In cell in preparation for the next doping level shown at a depth from 1.8 μm to 2.8 μm.

developing optoelectronics devices in the infrared spectral region. Indeed, a doping concentration from low 10^{15} cm^{-3} to higher than 10^{18} cm^{-3} can be easily achieved by using elemental indium (n-type) and arsenic (p-type) across the range of Cd mole fractions necessary to produce short- to long-wave infrared devices.

For indium doping, we use a traditional Knudsen effusion cell as described in Ref. 13. Figure 5 displays a SIMS scan from a calibration layer of In doping for LWIR material. Both low and high doping levels are obtained in the same growth. Indium doping has been shown to be x value insensitive (in this study from $0.15 < x < 0.5$), i.e., for a given cell temperature we get the same doping level regardless of the x value. Indium doping is not growth temperature dependent in the typical growth range, from 170°C to 190°C, and is dependent only on the growth rate; for a fixed In source temperature, higher doping is obtained with lower growth rates. In Fig. 5, the higher background level shown for depths from 2.8 μm to 3.8 μm is due to the In cell that had its temperature increased for the next doping level shown at a depth from 1.8 μm to 2.8 μm.

Arsenic doping, on the other hand, has been shown to be sensitive to nearly all growth conditions. Several studies by different groups have

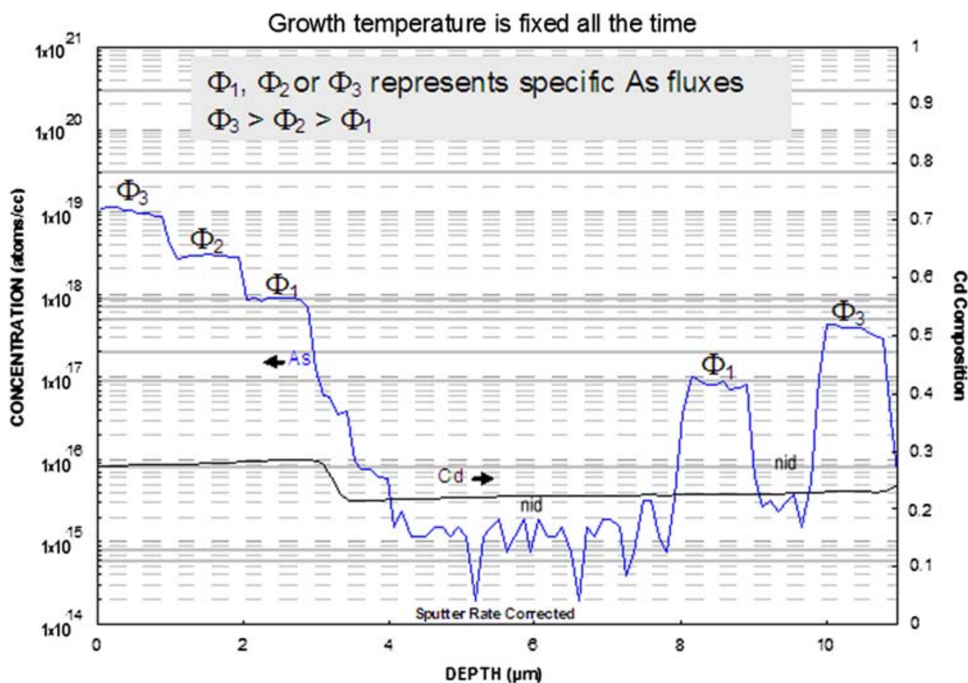

Fig. 6. Arsenic SIMS scan for a mid/long-wavelength material calibration growth. Φ_1, Φ_2, and Φ_3 represent specific As fluxes used for doping, where $\Phi_3 > \Phi_2 > \Phi_1$. *nid* = nonintentionally doped. The nonabrupt profile observed between a depth of 3 μm and 3.5 μm is caused by the higher incorporation of As with higher *x* value of $Hg_{(1-x)}Cd_xTe$ (As flux is kept constant in this region and equal to Φ_1). The growth temperature is constant during the layer growth.

reached this same conclusion.[14,15] Figure 6 shows an As SIMS scan for a mid/long-wavelength material calibration growth; the growth temperature is kept constant throughout the growth. We observe that, by using the same As flux during growth, a higher doping level is obtained for higher x-value material. In the figure, Φ_1, Φ_2, and Φ_3 represent specific As fluxes, where $\Phi_3 > \Phi_2 > \Phi_1$. More than one order of magnitude increase of the doping concentration is observed with the same As flux if we change the x value from 0.23 to 0.28. This phenomenon induces the nonabrupt profile observed on the SIMS scan in Fig. 6 between a depth of 3 μm and 3.5 μm, which is caused by the As flux kept constant in this region but with changing x value of $Hg_{(1-x)}Cd_xTe$. Also, the As incorporation is strongly enhanced with lower growth temperatures, as shown by other groups.[14,15]

The minimization of unwanted impurities is also vital for device performance. We have tested our material for most common impurities such as C, I, Cl, O, K, and Na, and all SIMS scans typically show concentrations below the limits of detection.

Electrical Activity

Having a SIMS scan showing that we have the doping element incorporated at the level targeted does not mean that all of the impurities are electronically active, i.e., that each impurity element is contributing at least one electron or hole to electrical conduction for n- or p-type, respectively. In order to measure the carriers which are electrically active, we use Hall-effect measurements and then compare the value measured with impurity concentrations determined by SIMS.

For Hall measurements, we use the traditional van der Pauw geometry[16,17] on structures that are composed of a single layer, with single doping concentration, single doping element, and a well-known thickness grown on a high-resistivity CdTe/Si substrate. The magnetic field used has a magnitude of 0.3 T. Hall measurements are performed as a function of temperature, from 300 K to 30 K.

We started this study by checking the growth chamber background doping level. $Hg_{(1-x)}Cd_xTe$ layers for different x values with nonintentional doping were grown and Hall-effect measurements were performed on them. Figure 7 shows a typical Hall data plot for our layers, showing n-type concentration in the low 10^{14} cm^{-3} range. The increase in the concentration for higher temperatures is compatible with calculated thermally generated carriers for this long-wave material (x = 0.23). The low concentration and high mobility (~50,000 cm^2/V s) at lower temperatures confirms the high-purity material grown. Also, it is shown in Fig. 7, that no major difference in the electronic properties is observed after annealing of the structure.

In Activity

As shown above, controlled n-type doping is achieved over a large range of concentrations in

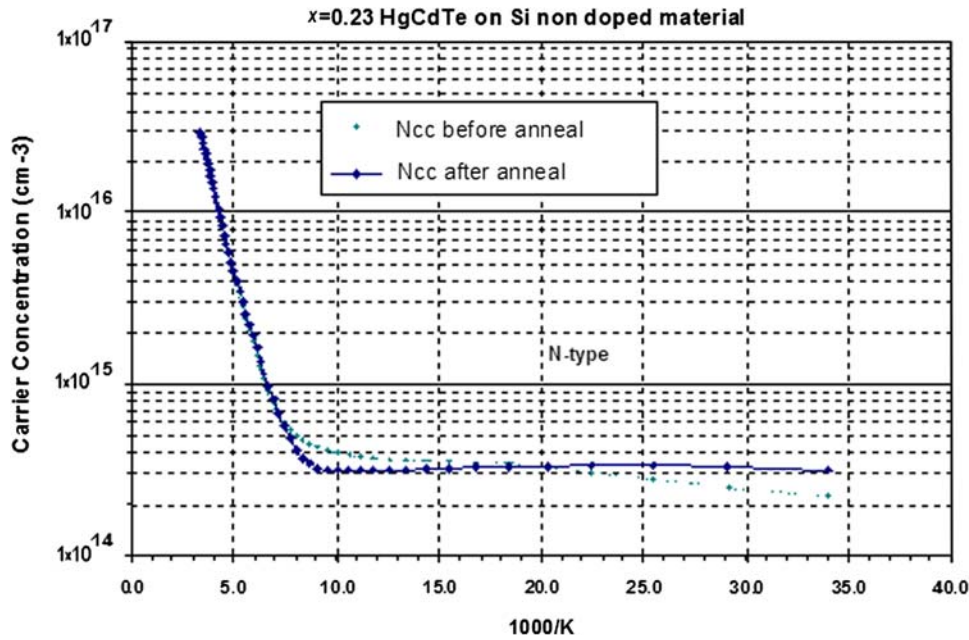

Fig. 7. Hall data plot of one unintentionally doped HgCdTe layer showing *n*-type concentration before and after annealing (mobility ~50,000 cm^2/V s). The increase in the concentration for higher temperatures is compatible with calculated thermally generated carriers for this long-wave material (x = 0.23).

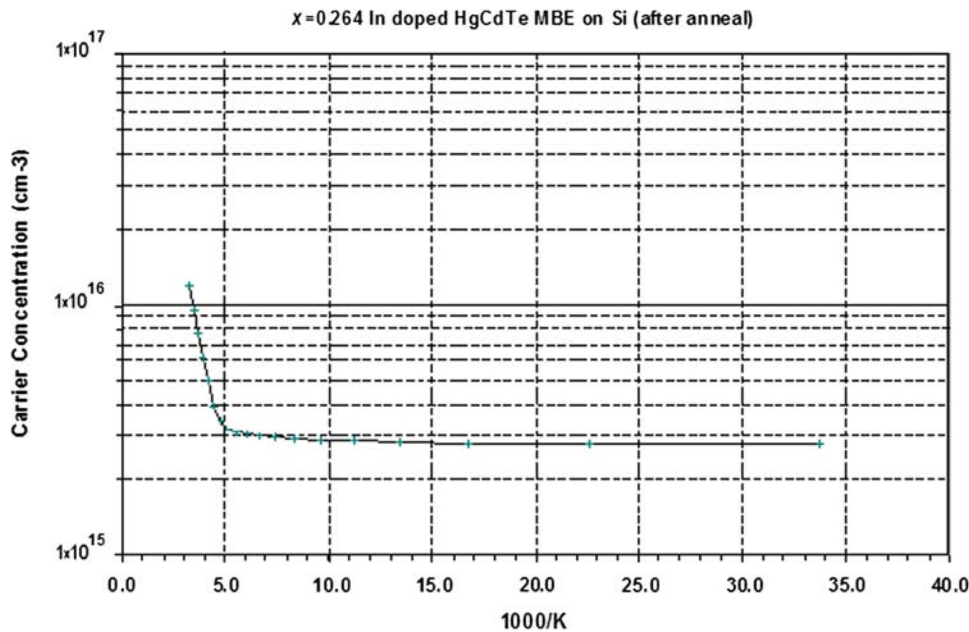

Fig. 8. Carrier concentration of one indium-doped mid-wavelength material (x = 0.264) obtained by Hall effect measured in an annealed sample (mobility ~85,000 cm^2/V s). For temperatures higher than 150 K (1000/K < 6.0) carriers thermally generated from intrinsic material start dominating the electrical conduction. SIMS scan performed on this layer shows indium doping concentration around 2.4×10^{15} cm^{-3}.

our MBE system. Figure 8 shows the carrier concentration of one of our mid-wavelength material growths (x = 0.264) obtained by Hall effect measured in an annealed sample. A flat carrier concentration around 2.8×10^{15} cm^{-3} is obtained for temperatures below 150 K (1000/K > 6.0) and for temperatures higher than 150 K (1000/K < 6.0), carriers thermally generated from intrinsic material start dominating the electrical conduction. This wafer had a SIMS scan performed, and an indium concentration around 2.4×10^{15} cm^{-3} was detected. The high quality of this n-type material is attested to by the high mobility measured, decreasing monotonically from 85,000 cm^2/V s for lower

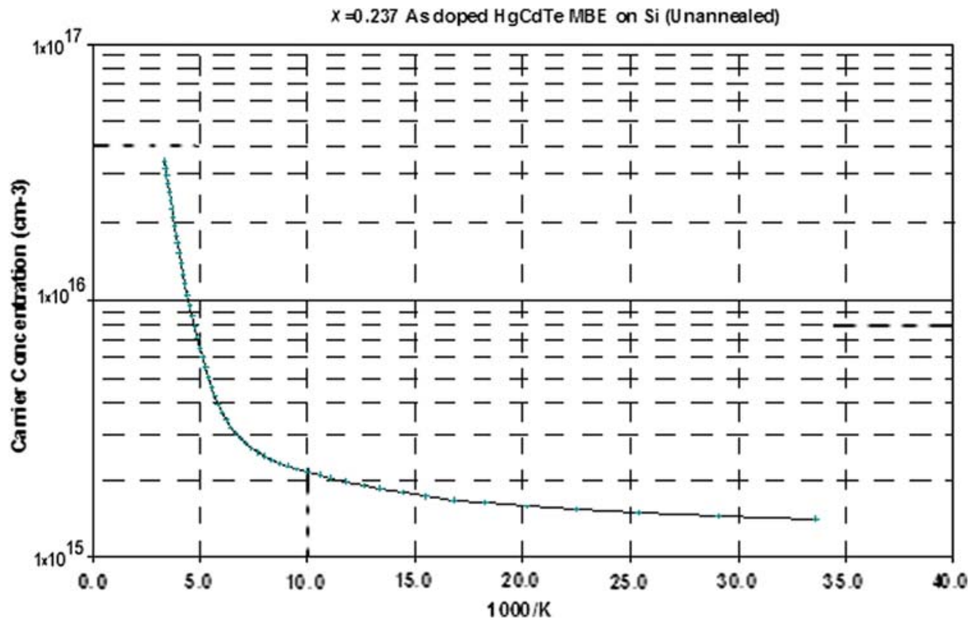

Fig. 9. The carrier concentration of an arsenic-doped long-wave material (x = 0.237) obtained by Hall-effect measurements, as grown. This layer is n-type with concentration of around 1.5 × 10^{15} cm^{-3} and mobility around 40,000 cm^2/V s. A SIMS scan performed on this layer shows arsenic doping concentration around 2.0 × 10^{17} cm^{-3}.

temperatures to 7000 cm^2/V s for higher temperatures. Comparable results are obtained for unannealed LW and SW material with 60,000 cm^2/V s for LW material and 17,000 cm^2/V s for SW material. After annealing, a minor improvement of the electrical properties (slightly higher mobility) is observed with no significant change in carrier concentration. We can thus affirm that 100% activation of carriers is obtained for all indium-doped wafers studied in this work.

As Activity

As explained in a previous section, controlled arsenic doping can be achieved over a wide range of concentrations in our MBE system. However, in contrast to indium, which behaves very well as an n-type dopant, arsenic has amphoteric behavior and with typical MBE HgCdTe growth conditions is incorporated as an n-type dopant. This phenomenon has been seen by other groups and is still a source of discussion.[15,18–21] One way to activate the arsenic as a p-type dopant is to anneal the layer under Hg pressure. Several works can be found in the literature modeling As activation[20,21] and detailing the procedure for annealing HgCdTe for this purpose[15,18–20] and will not be addressed in this work. Figure 9 shows the carrier concentration of one of our as-grown LWIR materials (x = 0.237) obtained by Hall-effect measurements. As we can see, the carrier type obtained is n-type and has a concentration of around 1.5 × 10^{15} cm^{-3} with mobility around 40,000 cm^2/V s. This layer has an arsenic incorporation of 2 × 10^{17} cm^{-3} atoms, as determined by SIMS. n-Type conduction with approximately 1% activation as determined by SIMS is typical for our layers as grown. For x values higher than 0.3, before annealing, the Hall measurements show that the arsenic is still n-type but with lower mobility values. The doped layer is electrically compensated, and higher x values produce lower mobilities.

Figure 10 shows a plot of the carrier concentration as a function of Arrhenius temperature on the same wafer shown in Fig. 9, but in this case after annealing. This layer is now p-type for temperatures lower than 190 K (1000/K > 5.2) with a concentration of around 4.0 × 10^{17} cm^{-3} and mobility around 130 cm^2/V s. For temperatures higher than 190 K (1000/K < 5.2), carriers thermally generated from intrinsic material start dominating the electrical conduction. As we can see, activation of more than 100% is obtained, since a carrier concentration of more than 4 × 10^{17} cm^{-3} is measured by Hall for lower temperatures, and SIMS of this same layer shows an arsenic incorporation of 2 × 10^{17} cm^{-3} atoms. This discrepancy can be explained by errors of measurements: ∼10% for Hall data and >15% for SIMS.[22] All the As doping studied here had carrier concentration in the 5 × 10^{16} cm^{-3} to 10^{18} cm^{-3} range, which is the doping region of interest. Similar results were obtained in all ranges of x values studied here, from x = 0.2 to x = 0.72. At arsenic doping levels above 10^{18} cm^{-3}, lower activation ratios have been observed by other groups.[18,19]

CONCLUSIONS

HgCdTe/Si has demonstrated very high potential as a cost-effective choice for producing large-area

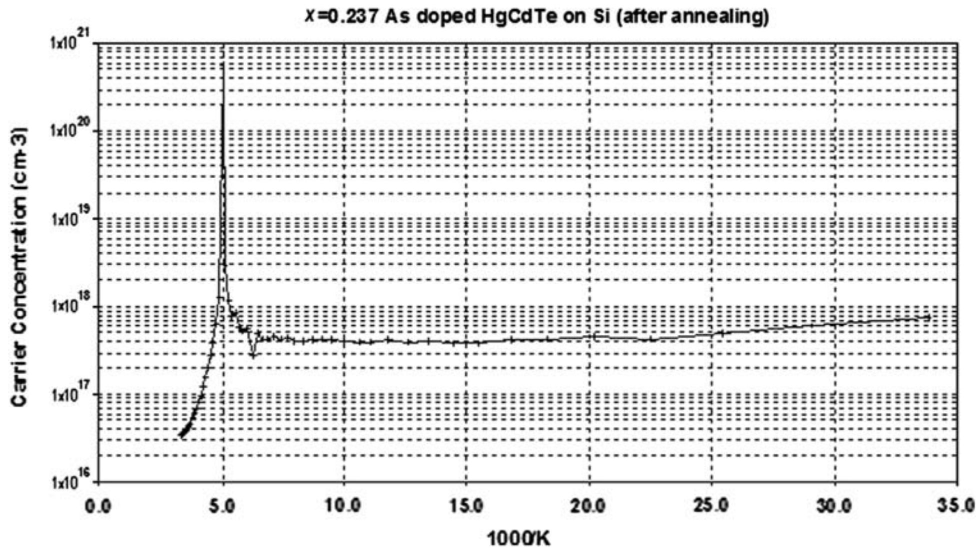

Fig. 10. Carrier concentration of the same arsenic-doped long-wave material ($x = 0.237$) shown in Fig. 9 after the activation anneal was performed, obtained by Hall effect. This layer is now p-type for temperatures lower than 190 K (1000/K > 5.2) with concentration of around 4.0×10^{17} cm^{-3} and mobility around 130 cm^2/V s. For temperatures higher than 190 K (1000/K < 5.2) carriers thermally generated from intrinsic material start dominating the electrical conduction.

HgCdTe devices. Despite the large lattice mismatch between HgCdTe and Si, it is shown that HgCdTe layers can be obtained reproducibly with very high uniformity and quality. MBE run-to-run compositional reproducibility is excellent using spectroscopic ellipsometry as a real-time feedback control. The versatility of the MBE technique and the broad area of the electromagnetic spectra covered by HgCdTe materials are an excellent combination for the fabrication of devices from SWIR to VLWIR, which are of great technological interest. High crystal quality is obtained for HgCdTe on Si, which is illustrated by x-ray rocking curves showing FWHM ~65 arcsec. Measured etch pit densities of grown material are approximately mid 10^6 cm^{-2} and independent of the x value. The macrodefect density is very low even after the growth of a very complex structure such as a two-color M-L detector structure. In addition, arsenic doping incorporation is easily obtained from low 10^{15} cm^{-3} to more than 10^{18} cm^{-3}, as determined by SIMS. The doping activity studied here was in the region of interest, from 5×10^{14} cm^{-3} to 10^{18} cm^{-3}. Indium and arsenic activation are obtained with approximately 100% activation, independent of the x value (as measured by SIMS and Hall-effect measurements in this range of interest). Both p-type and n-type doping was well behaved across all x values studied here (indium doping was studied from $x = 0.15$ to $x = 0.5$, and arsenic doping was studied from $x = 0.2$ to $x = 0.72$). It has to be noted that As doping behaves well after the activation annealing of the layer grown is performed. The quality of the p–n junction is validated by the performances of detectors in the LWIR[12,23,24] and MWIR[3] ranges, as previously reported. Short-wave avalanche photodetector (APD) results were recently obtained and will be published elsewhere.

REFERENCES

1. R. Sporken, S. Sivananthan, K.K. Mohavadi, G. Monfroy, M. Boukerche, and J.P. Faurie, *Appl. Phys. Lett.* 55, 1879 (1989). doi:10.1063/1.102159.
2. T.J. de Lyon, R.D. Rajavel, J.E. Jensen, O.K. Wu, S.M. Johnson, C.A. Cockrum, and G.M. Venzor, *J. Electron. Mater.* 25, 1341 (1996). doi:10.1007/BF02655030.
3. M.F. Vilela, A.A. Buell, M.D. Newton, G.M. Venzor, A.C. Childs, J.M. Peterson, J.J. Franklin, R.E. Bornfreund, W.A. Radford, and S.M. Johnson, *J. Electron. Mater.* 34, 898 (2005). doi:10.1007/s11664-005-0039-z.
4. M. Reddy, J.M. Peterson, D.D. Lofgreen, J.J. Franklin, T. Vang, E.P.G. Smith, J.G.A. Wehner, I. Kasai, J.W. Bangs, and S.M. Johnson, *J. Electron. Mater.* 37, 1274 (2008). doi:10.1007/s11664-008-0428-1.
5. J.B. Varesi, A.A. Buell, J.M. Peterson, R.E. Bornfreund, M.F. Vilela, W.A. Radford, and S.M. Johnson, *J. Electron. Mater.* 32, 661 (2003). doi:10.1007/s11664-003-0049-7.
6. A.A. Buell, L.T. Phan, M.D. Newton, G.M. Venzor, E.M. Norton, E.P. Smith, J.B. Varesi, V.B. Harper, S.M. Johnson, R.A. Coussa, T.J. de Lyon, J.A. Roth, and J.E. Jensen, *J. Electron. Mater.* 33, 662 (2004). doi:10.1007/s11664-004-0064-3.
7. K.D. Maranowski, J.M. Peterson, S.M. Johnson, J.B. Varesi, A.C. Childs, R.E. Bornfreund, A.A. Buell, W.A. Radford, T.J. de Lyon, and J.E. Jensen, *J. Electron. Mater.* 30, 619 (2001). doi:10.1007/BF02665844.
8. D.D. Edwall, M. Zandian, A.C. Chen, and J.M. Arias, *J. Electron. Mater.* 26, 493 (1997). doi:10.1007/s11664-997-0183-8.
9. T.J. de Lyon, R.D. Rajavel, J.A. Roth, and J.E. Jensen, *Handbook of Infrared Detection Technologies*, Chapter 9, ed. M. Henini and M. Razeghi (Elsevier Science Ltd., 2002), pp. 321–322.
10. T. Colin and T. Skauli, *J. Electron. Mater.* 26, 688 (1997). doi:10.1007/s11664-997-0217-2.
11. http://www.augusttech.com/InspectionProduct_ProductNSX.aspx.
12. S.M. Johnson, A.A. Buell, M.F. Vilela, J.M. Peterson, J.B. Varesi, M.D. Newton, G.M. Venzor, R.E. Bornfreund,

W.A. Radford, E.P.G. Smith, J.P. Rosbeck, T.J. de Lyon, J.E. Jensen, and V. Nathan, *J. Electron. Mater.* 33, 526 (2004). doi:10.1007/s11664-004-0041-x.

13. S.A. Barnett and I.T. Ferguson, *Handbook of Thin Film Process Technology*, ed. D.A. Glocker and S.I. Shah (Institute of Physics Publishing, 1995), ISBN 0 7503 0311 5, A2.0:5.
14. B.Z. Nosho, J.A. Roth, J.E. Jensen, and L. Pham, *J. Electron. Mater.* 34, 779 (2005). doi:10.1007/s11664-005-0020-x.
15. G.K.O. Tsen, R.H. Sewell, A.J. Atanacio, K.E. Prince, C.A. Musca, J.M. Dell, and L. Faraone, *Semicond. Sci. Technol.* 23, 015014 (2008). doi:10.1088/0268-1242/23/1/015014.
16. L.J. van der Pauw, *Philips Res. Rep.* 13, 1 (1958).
17. W.S. Knodle and R. Chow, *Handbook of Thin-Film Deposition Processes and Techniques*, ed. K.K. Schuegraf (Noyes Publication, 1988), ISBN 0 8155 1153 1, 206.
18. P. Boieriu, C.H. Grein, H.S. Jung, and J. Garland, *Appl. Phys. Lett.* 86, 212106 (2005). doi:10.1063/1.1940119.
19. M. Zandian, A.C. Chen, D.D. Edwald, J.G. Pasko, and J.M. Arias, *Appl. Phys. Lett.* 71, 2815 (1997). doi:10.1063/1.120144.
20. P. Capper and D. Shaw, *Proceedings of SPIE*, ISSN 0277-786X, CODEN PSISDG, 6294, 62940 M.1-62940M.12, 2006.
21. D. Shaw, *Semicond. Sci. Technol.* 23, 085014 (2008).
22. L. Wang, L.H. Zhang, and J. Li, *J. Electron. Mater.* 28, 793 (1999). doi:10.1007/s11664-999-0072-4.
23. M.F. Vilela, D.D. Lofgreen, E.P.G. Smith, M.D. Newton, G.M. Venzor, J.M. Peterson, J.J. Franklin, M. Reddy, Y. Thai, E.A. Patten, S.M. Johnson, and M.Z. Tidrow, *J. Electron. Mater.* 37, 1465 (2008). doi:10.1007/s11664-008-0443-2.
24. R. Bornfreund, J.P. Rosbeck, Y.N. Thai, E.P.G. Smith, D.D. Lofgreen, M.F. Vilela, A.A. Buell, M.D. Newton, K. Kosai, S.M. Johnson, T. de Lyon, J.E. Jensen, and M. Tidrow, *J. Electron. Mater.* 36, 1085 (2007). doi:10.1007/s11664-007-0177-6.